Available online at www.sciencedirect.com
ScienceDirect
Journal of Marine Systems 68 (2007) 201–214
JOURNAL OF MARINE SYSTEMS
www.elsevier.com/locate/jmarsys

The areas and ice production of the western and central Ross Sea polynyas, 1992–2002, and their relation to the B-15 and C-19 iceberg events of 2000 and 2002

Seelye Martin [a,*], Robert S. Drucker [a], Ronald Kwok [b]

[a] University of Washington, School of Oceanography Box 357940, Seattle, WA 98195-7940, United States
[b] Jet Propulsion Laboratory, California Institute of Technology, 4800 Oak Grove Drive, Pasadena, CA 91109, United States

Received 20 June 2006; received in revised form 11 November 2006; accepted 20 November 2006
Available online 18 January 2007

Abstract

For 1992–2002, the paper investigates the heat loss and area of three polynyas in the western and central Ross Sea. These are the Ross Sea Polynya (RSP) and the much smaller Terra Nova Bay and McMurdo Sound polynyas. The importance of these polynyas is that their associated salt rejection contributes to the formation of the High Salinity Shelf Water (HSSW) that is crucial to the Antarctic Bottom Water formation. The study divides into two parts, 1992–1999, when there was negligible iceberg activity, and 2000–2002, when major icebergs calved and interacted with the polynyas. To retrieve the ice thicknesses and heat fluxes within the polynyas, the paper uses an algorithm based on the ratio of the vertically and horizontally polarized Special Sensor Microwave/Imager (SSM/I) 25-km resolution 37-GHz channels, combined with meteorological data. Because of sidelobe contamination, the ice shelf and icebergs are masked. Our results show that for the polynyas, and consistent with other observations, their mean winter area is about 30,000 km^2 and their combined ice production is about 500 $km^3 y^{-1}$. We also find that the polynya ice production approximately equals the ice export. This is in contrast to the Weddell Sea, where the polynya ice production equals about 6% of the ice export. For the years 2000 and 2002, the calving of large icebergs directly affect the ice production by inhibiting the ice production off the shelf due to piling up of first year ice upwind of the bergs and by generating new polynyas downwind of the bergs. The period 1992–2001 exhibits an upward trend in polynya productivity. The decadal increase in the ice production suggests that the observed HSSW salinity decrease in the western Ross Sea is not due to the polynyas, but is rather due to a change in the properties of the water flowing into the Ross.

Keywords: Antarctic zone; Ross Sea; Sea ice; Polynyas; Icebergs

1. Introduction

The largest Antarctic polynya is the Ross Sea polynya (RSP), which forms in the central and western Ross Sea to the east of Ross Island, adjacent to the Ross Ice Shelf. The western Ross Sea also contains the Terra Nova Bay polynya, which is located immediately to the north of the Drygalski ice tongue, and a smaller polynya in McMurdo Sound. From a 5-year average (1997–2002), Arrigo and van Dijken (2003) show that the combined winter area of the RSP and McMurdo

* Corresponding author.
E-mail address: seelye@ocean.washington.edu (S. Martin).

0924-7963/$ - see front matter © 2007 Published by Elsevier B.V.
doi:10.1016/j.jmarsys.2006.11.008

polynyas is about 20,000 km^2, or an order of magnitude larger than any other Antarctic or Arctic polynya. Morales Maqueda et al. (2004) provide an excellent overview of the properties of polynyas in general, as well as providing brief descriptions of the RSP and Terra Nova Bay polynyas.

For the Ross Sea on April 6, 2000, Fig. 1 shows a wide swath synthetic aperture radar (ScanSAR) mosaic of the regional geography and the polynya locations. The RSP is made visible by the bright parallel wind-generated Langmuir streaks oriented at right angles to the ice shelf that are approximately parallel to the wind velocity. Consistent with (Arrigo and van Dijken, 2003, Fig. 2, Map 4), the figure shows that the polynya width varies from zero at the eastern edge of Ross Island at about 168°E to a maximum at about 172°E, then extends nearly across the entire ice shelf to about 160°W. Most of its area and activity, however, lie to the west of the date line. The figure also shows the location of the two smaller western Ross Sea polynyas, the McMurdo Sound (MAC) and the Terra Nova Bay polynyas (TNB). Finally, the image shows the just-calved giant iceberg B-15 and its companion B-17, and the location of what in 2002 will become iceberg C-19. (The naming convention of the National Ice Center (NIC) divides the Ross Sea into two sectors at 180°; B to the east, C to the west.) Both sets of bergs affect the RSP, but because C-19 calves directly into the widest part of the RSP, we show below that this berg and its companion, C-17, strongly affect the RSP production of ice and salt.

In the Ross Sea, the polynyas are a response to large-scale atmospheric winds and to the katabatic winds that form over the inland glaciers. Fig. 2 shows the ECMWF mean winter (April–November) surface pressure contours and the ice velocities determined from 85-GHz passive microwave feature tracking (Kwok, 2005, hereafter K05). The solid line across the Ross is the flux gate used in K05′s calculation of ice inflow and outflow, which Section 5 will compare with the ice production. The figure shows that there is a low-pressure system centered over the western Ross, which drives an ice inflow to the east and a strong ice outflow to the west. This ice and wind circulation help maintain the western Ross polynyas.

As Bromwich et al. (1993) describe, the RSP is also driven by the katabatic winds that form and flow north over the glacial outflows into the Ross Ice Shelf. These winds are diverted to the east of Ross Island and contribute to the formation of the RSP. For the winters of 1988–1991, Bromwich et al. (1998) show that, on average, about 60% of the RSP events are linked to katabatic surge events down the major glaciers. The

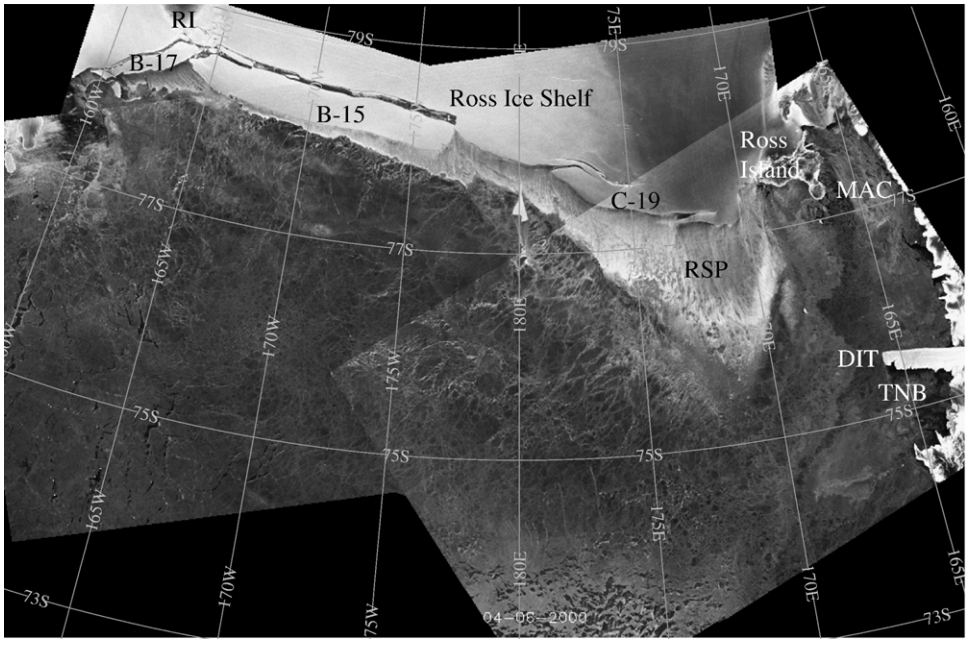

Fig. 1. RADARSAT ScanSAR image of the western Ross Sea, on April 6, 2000. South is up. The image shows the Ross Ice Shelf, the B-17 and B-15 icebergs, and identifies the region set off by a fracture that in 2002, becomes iceberg C-19. The image also shows the location of the Drygalski Ice Tongue (DIT), the Ross Sea polynya (RSP), the Terra Nova Bay polynya (TNB), the McMurdo Sound polynya (MAC), and the location of Ross and Roosevelt Island (RI). A characteristic 10-m air temperature at the center of the image is −15 °C, the 10-m wind velocity is 13 m s^{-1} from the south. RADARSAT image copyright by the Canadian Space Agency.

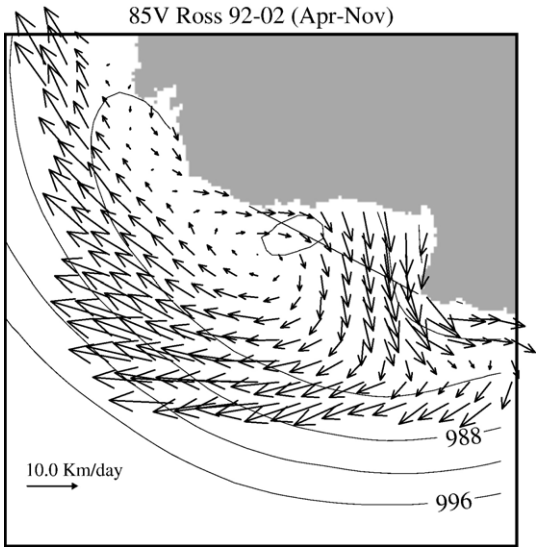

Fig. 2. Mean contours of sea level pressure in hPa and the mean ice export derived from the Special Sensor Microwave/Imagery (SSM/I) 85-GHz observations for April–November, 1992–2002. The contour interval for pressure is 4 hPa. The straight solid line shows the flux gate between Cape Adare and Land Bay (adapted from Kwok, 2005).

polynya size is also influenced by the warming associated with katabatic winds.

The importance of the RSP is at least two-fold. First, because the winter polynya consists of a large region of low ice concentration, in early summer it melts before the rest of the pack ice and generates a $\sim 10^5$ km^2 region of high biological primary productivity (Arrigo et al., 2002). Second, the water masses entering the region from the north and east from the Amundsen Sea, which consist of surface water, low-salinity shelf water and the Modified Circumpolar Deep Water (MCDW), circulate along the ice shelf and are modified by freezing, salt rejection and melting (Jacobs and Giulivi, 1998). Because of the winter freezing and salt rejection that occurs within the three western Ross polynyas, the densest water in the Ross Sea forms in the west. The most saline part of this dense water is the High Salinity Shelf Water (HSSW). The summer ice shelf sections given in Jacobs and Giulivi (1998, Fig. 3) show that the HSSW occurs between 160–180°E, or under the Ross polynya. Also, data presented in Jacobs et al. (2002) show that along the western Ross Ice Shelf between 1960 and 2000, the HSSW salinity decreased by about 0.1 psu. This decrease is large enough that the densest shelf water, which historically occurred in the southwest Ross, now occurs in the Weddell.

Jacobs et al. (2002) hypothesize that this decrease is due to changes in the upstream conditions, namely an accelerated melting of the Amundsen Sea ice shelves. In additional work, Assmann and Timmermann (2005) show from a numerical model that the interannual properties of the HSSW are determined by conditions in the Amundsen Sea. Both papers recognize the importance of the brine rejection in the Ross, but also state that the upstream conditions determine the variability. To understand the consequences of these changes in the HSSW, Jacobs and Giulivi (1998) recommend that particular efforts be made to determine the volume of sea ice exported from the continental shelf. This paper is a response to this recommendation, as well an attempt to investigate the role of iceberg calving on the ice production.

Following Carmack's (1986) definition, the HSSW has a salinity greater than 34.6 psu and a temperature within a few tenths of freezing. It has been directly associated with the Terra Nova Bay polynya (Van Woert, 1999), and the RSP. The importance of the HSSW concerns its contribution to the generation of the Antarctic Bottom water. First, in spite of an adverse topography, some of the HSSW may flow directly into the abyss (Budillon et al., 2003). Second, part of the HSSW flows under the Ross Ice Shelf, where the freezing point depression associated with the 400 m thick ice shelf causes the shelf to melt and consequently to dilute the HSSW, following which it rises up along the ice shelf bottom, where it generates the Ice Shelf Water (ISW) (Jacobs et al., 1979). This exits the ice shelf at about 175°W and flows north.

For 1992–2002, using a combination of passive microwave SSM/I 37 GHz observations and ECMWF meteorological data, the present paper describes an

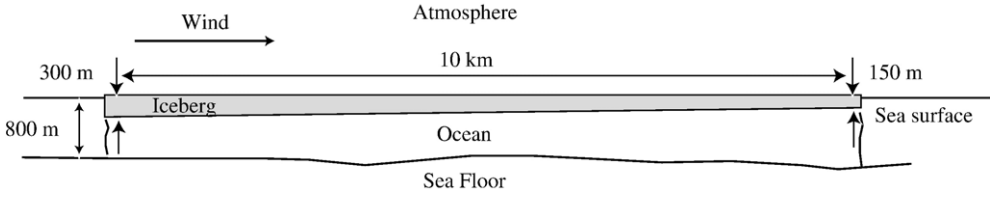

Fig. 3. Cross-section of a Ross Sea iceberg with the bottom depth and ice thickness approximately to scale. For B-15A, the iceberg width would be four times larger.

investigation of the size and the rate of sea ice production of the western Ross polynyas. Because the Advanced Microwave Scanning Radiometer (AMSR) data set begins with winter 2003, we restrict this study to the SSM/I and the period 1992–2002, but plan a future paper using the 12.5-km 36-GHz AMSR data. The organization of the paper is as follows. We begin with a discussion of the calving and physical properties of the icebergs and their behavior during the period 2000–2002. Our heat flux algorithm is then discussed, followed by the passive microwave masking of the icebergs and ice shelves. We then give the results of the heat flux calculations, and from comparison with K05, show that the polynya ice production and the ice export are in approximate balance. Finally, from comparison with published data, we show that the Weddell Sea exhibits a very different behavior.

2. Physical properties of the icebergs

As we show below and especially for the year 2000, the calving of icebergs from the ice shelf strongly affects the size and productivity of the polynyas. Keys et al. (1998) observe that although the ice shelf advances 0.9 km/year, for the period 1841–1997 the occurrence of sporadic calving events means that the ice shelf maintains a relatively stable geographic position. Prior to 2000, iceberg B-9, which calved in October 1987 and measured 150 km by 35 km, was the largest observed iceberg (Keys et al., 1990). Following B-9, there were no major calving events through 1997 (Keys et al., 1998), with the next large event being the B-15 calving in April 2000 (Arrigo and van Dijken, 2003). Given, as Keys et al. (1998) show, that the geographic position of the ice shelf front has remained approximately stationary over the past 160 years, we expect periodic calving of large icebergs. C. Hulbe (private communication, 2006) and Doake et al. (1998) suggest, by analogy with the Larsen Ice Shelf, that Roosevelt Island controls the ice edge position. North of the island, the ice strain rates are extensive, whereas south of the island, they are compressive. Because the region of extensive strains is unstable, it generates calving, so that as the ice advances beyond the island, icebergs form. This may be the reason that the edge of the ice shelf maintains a nearly constant position.

These bergs are very large. For example, B-15 measured approximately 300 km in length and 40 km in width, for an area of order 10^4 km^2. B-17 measured approximately 100 km in length, and 20 km in width. An aircraft radar survey shows that B-15 had a thickness gradient from the north side thickness of about 150 m to a south side thickness of about 280 m (D. Blankenship, private communication, 2005). The thickness gradient is associated with the summer melt of the underside of the ice shelf, and implies that on its south or windward side, the berg had a 30-m height above the waterline. Iceberg B-15 had a volume of 2700 km^3, a mass of $\sim 10^{15}$ kg, and a sail-to-volume ratio of 10^{-6} m^{-1}. The sail-to-volume ratio gives more of a sense of the relative effectiveness of the wind in transporting the berg, than the sail-to-draft ratio, which is constant for all bergs. A small ratio means that the large bergs are controlled not by the winds, but rather by currents, sea surface slope and collisions with topography and each other. Fig. 3, a cross-sectional cut of a Ross Sea berg drawn approximately to scale, schematically shows the dominance of the below-water portion of the iceberg. As Keys et al. (1990) describe for iceberg B-9, the effect of the sail-to-volume ratio is that the large icebergs drift with the currents and independently of the wind speed, so that the wind causes sea ice to accumulate on their upwind side and polynyas to form on their downwind side. As Section 5 shows, this means that in some cases the shelf polynya is suppressed on the upwind side of the bergs by the accumulated pack ice, while on the downwind side, new polynyas enhance the total production.

3. Iceberg behavior in 2000–2002

Because the berg positions and orientations determine the location and size of their associated downwind polynyas, and because, as we show in Section 4, sidelobe problems with the passive microwave heat flux algorithm require that the bergs be masked, we next examine the details of the drift and fracture of the icebergs.

For 2000 and 2002, we generated a time series of the berg positions using RADARSAT ScanSAR imagery and Moderate Resolution Imaging Spectroradiometer (MODIS) cloud-free infrared imagery. Because RADARSAT is primarily solar powered, there is no ScanSAR available for an approximate two-month period centered on the winter solstice, or for example, between May 11 and August 2, 2000. Even for periods when RADARSAT was operational, the SAR coverage was sporadic. In contrast, MODIS provided good coverage in May–August, but was hampered by increasing cloudiness during September–October. In spite of these problems, for the period April through early November during both years and with the exception of iceberg C-18, we obtained imagery of the icebergs at approximately weekly intervals. We geographically registered these images, then interpolated them to a daily time series, which we next discuss.

For 2000, Fig. 4 shows the outlines of the icebergs at 3-day intervals, superimposed on a MODIS infrared image on 15 April and on the bottom topography (Davey, 2004). For these icebergs, a critical topographic feature is the Ross Bank seamount (76.68 S, 179.23 E), which has a minimum depth of 170 m, or shallower than the B-15 depth on its southern side. The interaction of B-15A with this seamount causes it to have a different trajectory than other bergs, in that B-15A moves to the west along the ice shelf while the other bergs move north into the Southern Ocean.

In early April 2000, icebergs B-15 and B-17 calved respectively to the west and east of the fracture zone north of Roosevelt Island. On 10 May 2000, as B-15 drifted north and west, it fractured into two equally sized bergs, B-15A to the west and B-15B to the east. On about June 6, B-15A crossed the date line, and encountered the southward-flowing geostrophic current on the east side of Ross Bank (Van Woert et al., 2003, Fig. 16). The effect of this current combined with a collision with B-15B meant that the western end of B-15A rotated south, such that its western edge moved south and west of the seamount. While B-15A rotated and moved west, B-17 and B-15B moved north, consistent with the 1987–89 observed northward flow of iceberg B-9 in the same region (Keys et al., 1990). On August 6, B-15D calved from the east end of B-15A when it may have struck the seamount (Given that the northern end of B-15A is shallower than the seamount depth, and that the time series is at 3-day intervals, we do not have imagery of the details of the berg interaction with the seamount). Since the seamount prevented B-15A from moving north, it drifted in the westerly current along the edge of the ice shelf, while the other bergs drifted northwest. Although not shown on the figure, B-15A continued to move west until its western end grounded against Ross Island. The berg then rotated until its long axis was oriented north–south, where its southern end remained grounded and its northern end oscillated with the tides and currents.

In 2001 and 2002, the southern end of iceberg B-15A remained grounded against Ross Island with its long axis oriented north–south, and its northern end free to oscillate. Because of its location and orientation, B-15A served as the western limit of the RSP. We determined its daily winter 2001 and 2002 positions from data provided by Douglas MacAyeal, who had placed two GPS units on the berg, and from these, provided us with a daily time series of the B-15A position. No other large icebergs calved in 2001.

The year 2002 involved three icebergs: B-15A, C-18 and C-19. Fig. 5 shows the outlines of the bergs at 3-day intervals starting on 11 May, superimposed on the bottom topography and on a MODIS infrared image for 26 April 2002. The region shown is to the west of that shown in Fig. 4. The reason for the choice of 26 April as

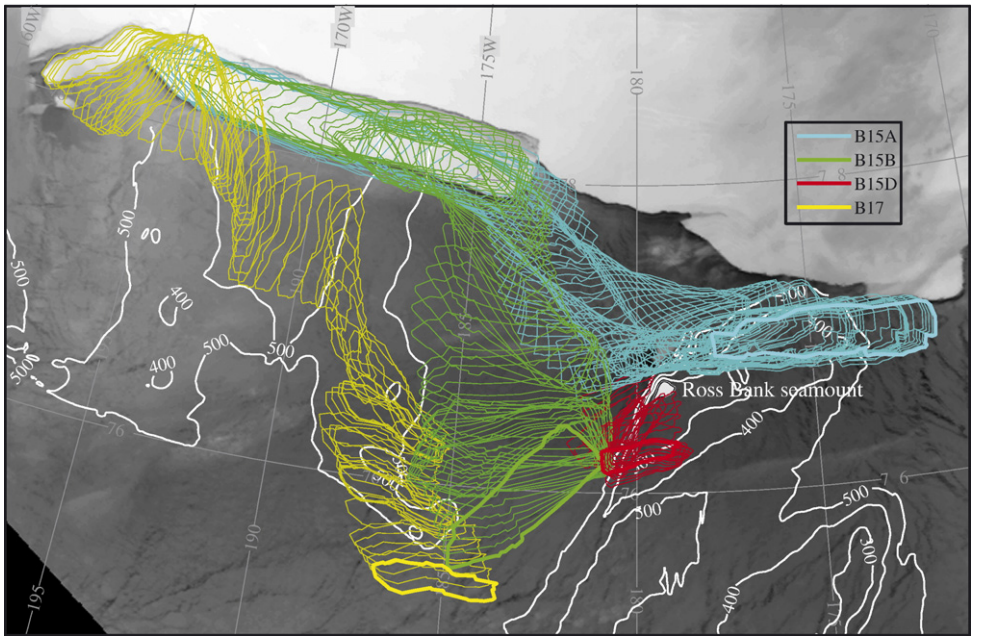

Fig. 4. Locations at 3-day intervals of the outlines of the icebergs B-15, B-15A, B-15B, B-15D, and B-17, for the period 15 April 2000 to 7 November 2000, overlain on the Davey (2004) ocean bottom topography and on a 15 April 2000 MODIS image. See text for further discussion.

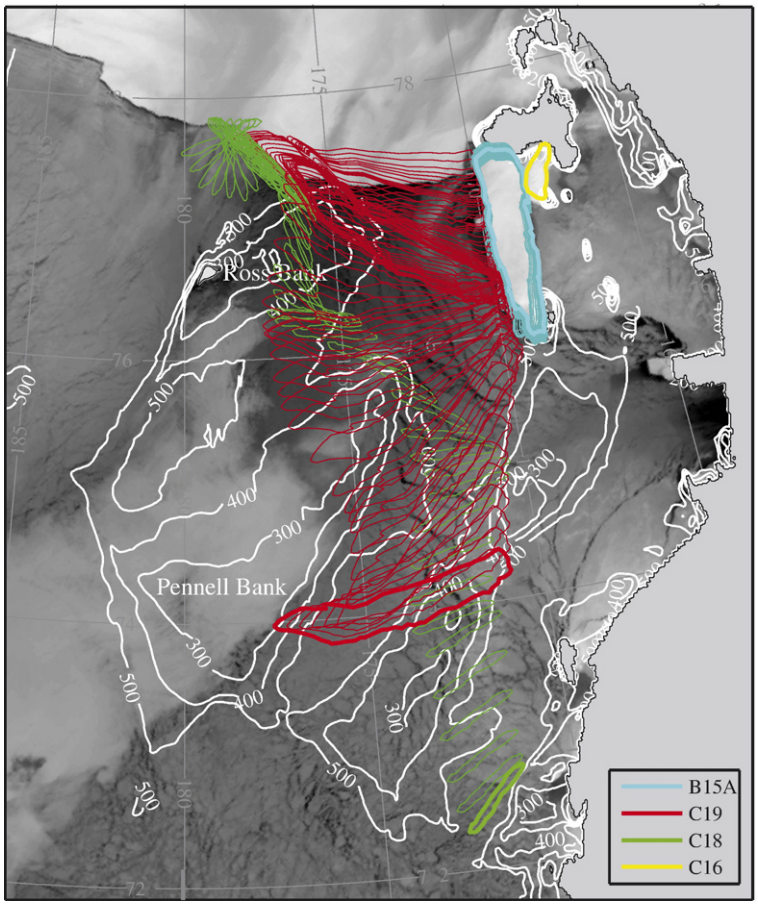

Fig. 5. Locations at 3-day intervals of the outlines of the icebergs B-15A, C-18 and C-19 for 2002 during the period 11 May 2002 to 7 November 2002, overlain on the Davey (2004) ocean bottom topography and on a MODIS image from 26 April 2002. See text for further discussion.

a background image was that the early images in the time series were very cloudy, and the 26 April image was one of the first clear sky images acquired immediately before or during the calving event. On about May 5, 2002, berg C-19, which measured 30 km wide by 200 km long, and the much smaller C-18, which measured 6 km wide by 70 km long, broke off from the ice shelf between 170 and 180°E, following which both bergs moved north. As the figure shows, after an initial 180° rotation of C-18, the long axes of C-18 and C-19 tended to remain approximately parallel to the ice shelf and perpendicular to the wind direction. Although the C-19 time series ends on 7 November, the final position for C-18 is 11 October. Following this time, heavy clouds hid its position. The figure also shows the envelope of the B-15A displacement.

The April 2000 ScanSAR image in Fig. 1 shows that the shelf ice that will become C-19 lies directly in the formation region of the RSP. Because large bergs such as C-19 are advected primarily by the currents and not by the wind, whereas the ice is advected by both winds and currents, new polynyas form downwind of the bergs; simultaneously, C-19 suppresses the growth of the RSP by trapping the wind-advected pack ice between the berg and the ice shelf. In contrast, the smaller C-18 moved downwind faster than C-19, and probably had a wind advection component to its velocity.

As an example of the downwind formation of polynyas and the upwind trapping of ice by the bergs, for 22 September 2002, Fig. 6 shows a MODIS thermal-infrared image (band 32) of the western Ross Sea. In the center of the image, the 2-m air temperature is −25 °C and the wind velocity is southwest at 18 m s^{-1}. The bright areas are warm thin ice, while the dark areas are either thick pack ice, glacier ice or clouds, all of which have a colder surface than the polynyas. The letter ‘A’ marks a region of first year ice that accumulates to the south of C-19 with a north–south width of order of the berg length. As our discussion of Fig. 10 shows below, although the winds are optimized for polynya growth,

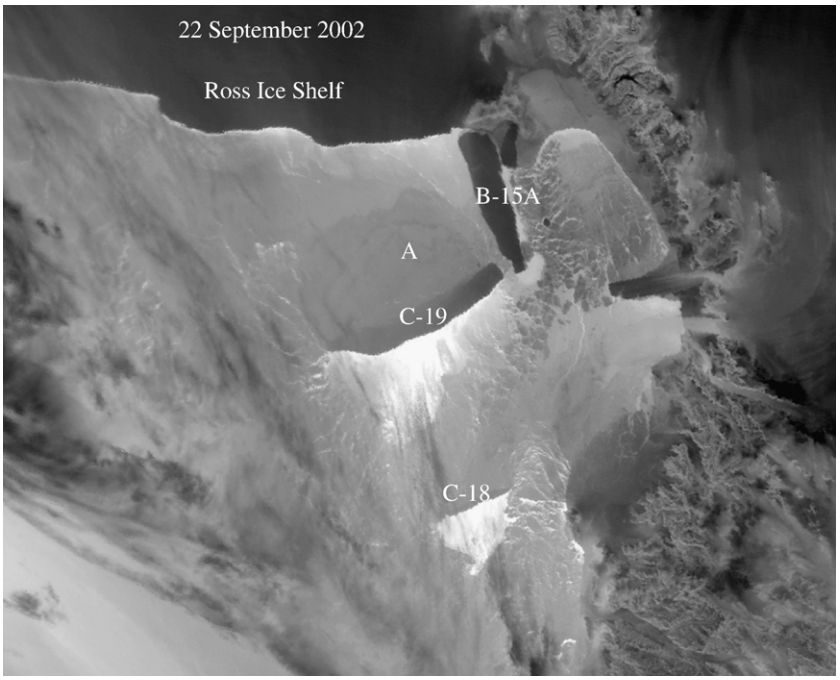

Fig. 6. MODIS infrared image (band 32) of the western Ross Sea on September 22, 2002. The light areas on the image are warm; the dark are cold. The 10-m air temperature is −25 °C and the 10-m windspeed is 18 m s^{-1}. The letter 'A' marks a region of first year ice that is trapped south of C-19. See text for further description.

this trapped first-year ice provides a mechanism for suppression of the shelf polynya. The image also shows polynyas occurring downwind of C-18 and C-19.

4. Calculation of the polynya heat flux

Our calculation of the polynya heat loss is based on the passive microwave thin ice algorithm developed for the Chukchi Sea and described in Martin et al. (2004). This thin ice algorithm depends on the change in surface salinity with ice thickness that occurs for thin ice, and derives the ice thickness with a nominal pixel size of 25 km × 25 km from the ratio of the 37 V and 37 H gridded brightness temperatures. This algorithm is validated with ice thickness data derived from AVHRR surface temperatures for the Langmuir-like circulations shown in Fig. 1. As Martin et al. (2004) show, because the restriction of this algorithm to thicknesses of 10 cm or less captures about 90% of the polynya heat loss, we define the polynya as the ice contained within the 10-cm contour. The retrieved thicknesses are then combined with a bulk coefficient meteorological heat flux algorithm described in Drucker et al. (2003) to derive the heat loss. In the calculation, we assume that the water column is at the freezing point, so that the atmospheric heat loss yields the ice growth. Given that the seawater is ice-covered before the polynya forms, this seems like a reasonable assumption. For all the polynyas, we interpolate the heat flux from the ECMWF 2-m temperatures and the 2-m winds derived from the ECMWF surface level pressures.

In our application of the SSM/I algorithm, we observed that sidelobe contamination made a portion of the adjacent shelf or icebergs appear to be part of the polynyas. To understand this contamination, we examined the distribution of the 37-GHz brightness temperatures. We found that away from the shelf or glacial ice edge, the ice shelves and icebergs have a lower brightness temperature than the polynyas, while adjacent to the polynyas, the warmer polynya brightness temperatures made the adjacent glacial ice appear warm, which increases the apparent area of the polynyas. We eliminated these false polynya regions by masking the ice shelf and bergs. For the ice shelf, given the 25-km resolution of the SSM/I and its slow rate of ice shelf advance, we determined the location of the shelf edge from three images. For dates prior to 19 March 2000 when B-15 calved, we used a ScanSAR image from 20 September 1998. After this date, we used a ScanSAR image from 1 April 2000. Finally, for dates after 14 May 2002 when C-19 calved, we modified the western portion of the 1 April 2000 ScanSAR image using a

MODIS image from 18 July 2002. For the icebergs, we masked the passive microwave imagery using the time series discussed in the previous section.

As an example of the application of our heat flux algorithm to the drifting bergs, for 24 August 2000, Fig. 7 compares the spatial distribution of the heat fluxes derived from MODIS and the masked SSM/I images. The upper panel shows the MODIS heat flux derived at a 1-km scale from channels 31 and 32 using the Key et al. (1997) Ice Surface Temperature (IST) MODIS algorithm as adapted for the Antarctic sea ice (http://stratus.ssec.wisc.edu/products/surftemp/surftemp.html). On this website, there is a caution that the "MODIS coefficients have not been tested." Although Hall et al. (2004) discuss the accuracy of the Arctic MODIS algorithm, there has been no equivalent discussion of the Antarctic sea ice algorithm. The lower panel shows the SSM/I heat flux, where the white blocks represent the masked icebergs, ice shelf and land, and where we mask any pixel that is more than 20% covered by glacier ice. For the icebergs,

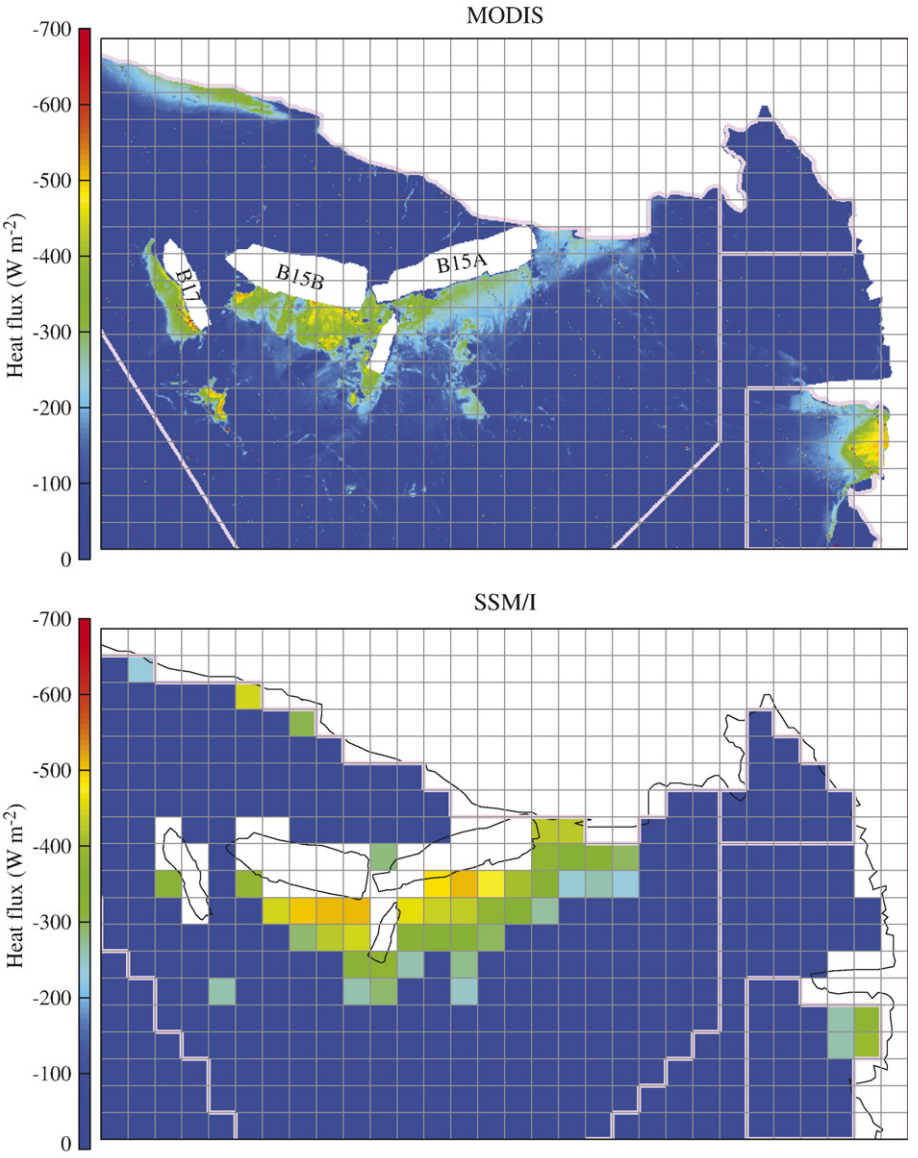

Fig. 7. Comparison of the heat fluxes derived from MODIS (upper panel), and the SSM/I fluxes (lower panel) with the berg and ice shelf masks applied, for 24 August 2000. The characteristic 10-m wind speed is 7.6 m s^{-1} from southwest, the 10-m air temperature is −29.2 °C. The rectangular grid shows the SSMI pixels; white corresponds to the MODIS and SSM/I ice shelf and iceberg mask. See text for further description. (For interpretation of the references to colour in this figure legend, the reader is referred to the web version of this article.)

the masks are calculated and applied daily. The pink lines outline the areas used in the calculation of the heat loss from the three different polynyas.

The MODIS image shows that regions of heat flux exist adjacent to the ice shelf and downwind of the icebergs. There is also a strong polynya in Terra Nova Bay. The SSM/I image in the lower panel shows that the same polynyas that occur in the MODIS image are visible at a reduced resolution. In spite of the coarse SSM/I resolution, both panels show a similar pattern of heat losses. Because of the wind accumulation of thicker ice south of the bergs, this region has a low heat flux. The agreement is not perfect; the upper image shows that the Terra Nova Bay polynya has a large heat flux, whereas it is smaller in the SSM/I image. The reverse holds for the polynyas downwind of the icebergs and ice shelf. This difference is probably due to the following. First, as Hall et al. (2004, page 1076) observe, the presence of "even very thin clouds or fog" can make it impossible to obtain an accurate IST. Second, because the MODIS image is a snapshot taken at a single time, whereas the SSM/I is the average of at least two passes, separated by about 12 h, the two images are not equivalent. Finally, the figure also shows that the combined length of icebergs B-17, B-15B and B-15A provides an extended boundary for a large offshore polynya. As the next section shows, this geographic configuration contributes to the conditions for a large offshore ice production.

Martin et al. (2004) discuss the accuracy of the masked SSM/I-derived heat loss. Its accuracy depends on two factors, the accuracy of the heat flux algorithm, and the accuracy of the polynya area associated with the coarse pixel resolution. As Fig. 7 shows, because the 25-km mask by necessity excludes a portion of the adjacent water and thin ice, the masked images underestimate the polynya area. Also, because the associated systematic error depends on the polynya area measured in the number of pixels, it is difficult to estimate this error, since it varies from image to image. For small polynyas of only 1–3 pixels, the error is large, probably of order 100%. For larger polynyas, it is smaller. In their series of comparisons of areas and heat fluxes determined from AVHRR and SSM/I images of the same polynya from the Alaskan coast of the Chukchi Sea, Martin et al. (2004) find that for a polynya consisting of about 15 pixels, or 10,000 km^2, the area is underestimated by about 30%. Since as we show below, the RSP has a mean area of about 25,000 km^2, its systematic error is probably less than 30%. For the total heat loss, Martin et al. (2004, their Fig. 9) found that when a series of AVHRR and SSM/I polynya images were masked identically, the root-mean-square difference between the two sets of heat losses was about ±16%.

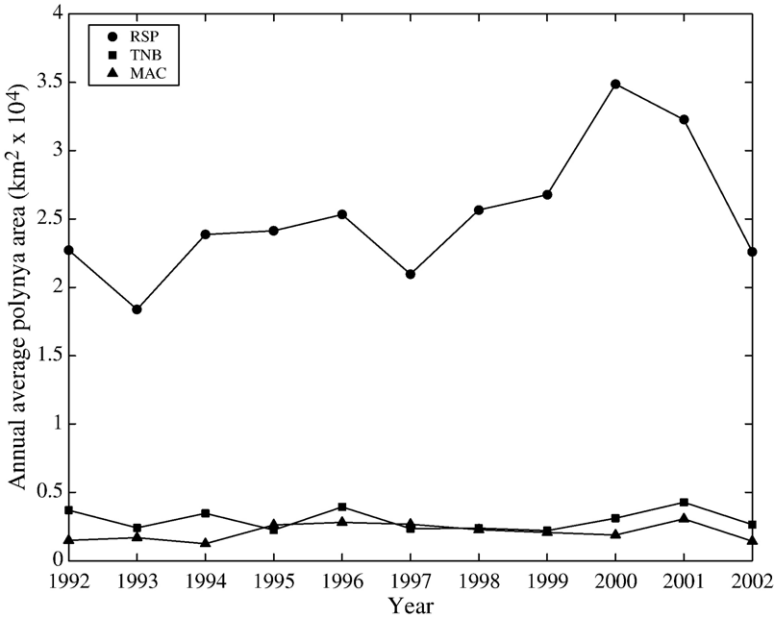

Fig. 8. Annual average polynya areas for the three western Ross Sea polynyas. RSP is the Ross Sea polynya, TNB is Terra Nova Bay and MAC is McMurdo Sound. See text for further description.

5. Results

From the ice thickness algorithm, Fig. 8 shows the average winter area for each of the polynyas. We define winter as lasting from the time when the ice cover fills our region of interest to when the pack ice starts to decay. For each year, Table 1 shows the start and stop days of our time series and the duration of our observational period. The areas are calculated from the masked SSM/I images and averaged over all winter days. For 2000 and 2002, the RSP area includes the polynyas downwind of the icebergs.

For all years, the figure shows that the RSP is an order of magnitude larger than either of the other polynyas. The RSP has its maximum mean area in 2000, which is the B-15 year, and its minimum in 1993. For 1992–2002, the mean RSP area is 25,000 ± 5000 km^2; the TNB area is 3000 ± 750 km^2 and the MAC area is 2000 ± 600 km^2, so that the combined areas of the TNB and MAC are about 20% of the RSP. For the RSP area, Zwally et al. (1985) use the Scanning Multichannel Microwave Radiometer (SMMR) data to find a mean area of 25,000 km^2, which agrees with our result. In more recent work, for June–October, 1997–2001, Arrigo and van Dijken (2003) use the passive microwave algorithm of Markus and Burns (1995) to calculate the average June–October open water area in the western Ross Sea, which from their Fig. 2, Map 4, includes the RSP and McMurdo polynyas, but excludes Terra Nova Bay. Their algorithm has a 6.25-km resolution; their threshold for defining a pixel as belonging to a polynya is that the pixel has a sea ice concentration less than 10%. Without masking the icebergs and ice shelf, they find a winter mean area of 20,000 km^2, with no error bars given. For the same years, but averaging over our two-month longer period of April–October, we find a mean area for these polynyas of 27,000 ± 5000 km^2. The difference between the two estimates is probably explained by their absence of error bars, the fact that our time series begins in April, not June, and that their 10% ice concentration isopleth does not necessarily correspond to our 10-cm polynya boundary. In a further comparison for Terra Nova Bay, Van Woert (1999) cites AVHRR observations from Kurtz and Bromwich (1983, 1985) showing that this polynya has an average winter area of 1300 km^2, compared to our 3000 ± 750 km^2. Given the difficulty of estimating polynya area from the AVHRR and the coarseness of our SSM/I resolution, these numbers are comparable.

Table 1
Start and stop days and number of days for the calculations of the area and heat loss of the Ross Sea polynyas

Year	Start day	Stop day	Number of days
1992	92	309	218
1993	97	300	204
1994	91	288	198
1995	87	314	228
1996	100	314	215
1997	91	304	214
1998	91	290	200
1999	91	304	214
2000	93	312	220
2001	96	304	209
2002	98	311	214

In the non-leap years, day 91 corresponds to April 1; day 300 to October 27.

For the 11-year period and for the different years identified by the inset scale, Fig. 9 shows the mean monthly heat loss of the RSP in km^3 of freshwater ice. For each month, the heavy solid line shows the mean, the dashed lines show the standard deviation. The light solid lines connect the data points for iceberg years of 2000 and 2002. The mean monthly ice production curve shows that, with the exception of a slight increase during September, the monthly values are nearly constant. For each month, the standard deviation is about ±25 km^3. The largest monthly value occurs in August 1998 at 150 km^3, which is more than twice the mean. From examination of the daily SSM/I imagery, the August 1998 value is consistent with the observed large RSP area that occurs in this month. For the seven-month winter mean, the total heat loss corresponds to 400 ± 65 km^3 yr^{-1}; 40% of which occurred in April–May–June, and 50% in July–August–September.

The iceberg years of 2000 and 2002 marked by the thin solid lines show a different behavior. For 2000, the winter average heat loss corresponds to 530 km^3 yr^{-1}, or almost two standard deviations greater than the mean, but with about 30% of the loss in April–May–June and 60% in July–August–September. In 2002, the winter average heat loss is 350 km^3 yr^{-1}, and the balance observed in 2000 is reversed, with 50% of the loss in April–May–June and 40% in July–August–September.

To illustrate how the presence of icebergs affects the ice production, Fig. 10 shows the daily cumulative production for 2000, 2002 and for all years. For the iceberg years of 2000 and 2002, the daily cumulative ice production is divided into four parts. These are the total cumulative production (closed circles), the production downwind (north) of the bergs (inverted triangles), the production off the shelf that is not upwind (south) of any berg (triangles), and the shelf production upwind (south) of the bergs (diamonds). As before, the berg and shelf pixels are masked. For 2002, because C-19 remains part of the shelf until about 1 May, the berg polynya series does

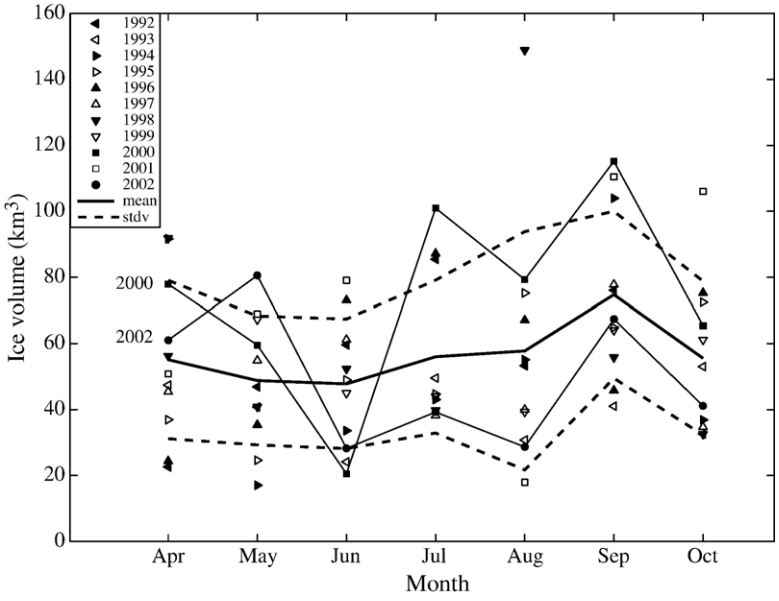

Fig. 9. The mean monthly RSP ice production for the period 1992–2002 for the different years identified by the inset scale, and the mean (heavy solid line) and standard deviation (dashed lines). The iceberg years of 2000 and 2002 are shown by the light solid lines. See text for further description.

not begin until this time. For comparison, the bottom figure shows the cumulative ice production for all years.

Beginning with 2000, the curves show in the period May–June that the ice production predominantly occurs downwind of the shelf. Then beginning about 1 July, as the bergs move to the west and offshore, the shelf cumulative production tends to level off while the production downwind of the bergs grows rapidly. The decrease in shelf production appears to occur because B-15A has moved west into the main region of the RSP and blocks its production. The figure also shows that the production between the bergs and the shelf is negligible. The steep increase in the berg production suggests that the bergs, and in particular, the irregular arrangement of B-17, B-15B and B-15A generates a longer coastline for the polynyas than the nearly straight shelf, so that the icebergs enhance the polynya productivity as they drift offshore. In the lower figure, comparison of the post-June steep growth of the 2000 total production with the non-iceberg years shows that this increase is unique to 2000.

For 2002, because iceberg C-19 calves directly in the middle of the region of strongest ice production, the ice production curves differ from 2000. First, until 1 May when C-19 calves, the total ice production and the shelf production are identical. After 1 May, the cumulative shelf production grows more slowly, while the bergs contribute the majority of the ice production, with only a negligible amount of production occurring between the bergs and the shelf. Because these bergs calve directly into the main body of the shelf polynya, they hamper its growth in the later part of winter. In the lower figure, examination of the 2002 total production shows no significant difference between its behavior and the other non-iceberg years.

We next discuss the behavior of the annual polynya ice production and compare it with an estimate derived from K05, which we derive as follows. As Fig. 2 shows, the K05 ice outflow from the Ross Sea has two components; the ice generated in the western Ross Sea and, to the east, the ice that enters the Ross Sea across the flux gate, circulates east-to-west, then exits to the west. Because K05 calculates both the inflow and outflow, we compare our estimate of the amount of ice generated in the western Ross Sea polynyas with the difference between the K05 inflow and outflow. To convert the K05 area flux to volume flux, we multiply the area by ice thickness measurements from Jeffries and Adolphs (1997). These measurements were made from shipboard in the western Ross Sea during May–June 1995, and consist of measurements of the thickness of ice floes tipped on their sides by the ship motion, where their Fig. 2 shows the mean and standard deviation of these thicknesses placed into 100-km wide latitudinal bins. Their other thickness data set was taken by ice coring, but because these were biased by the necessity of the ice being thick enough to work on, we used the shipboard measurements.

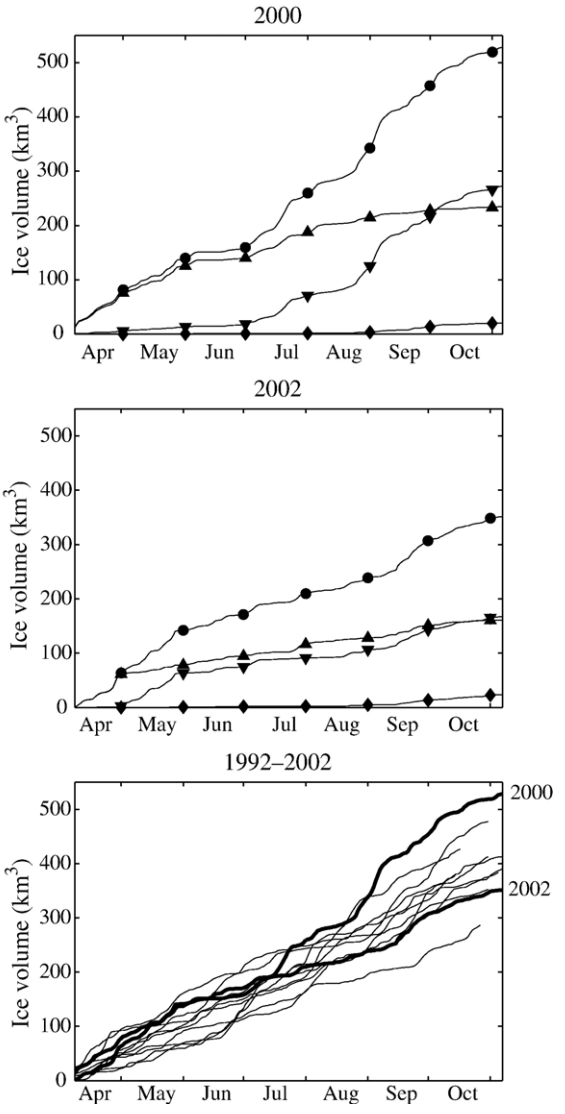

Fig. 10. The daily cumulative ice production for 2000 (upper figure), 2002 (middle) and 1992–2002 (bottom). On the upper two figures, the cumulative production divides into the total production (black circles), the production that occurs downwind (north) of the bergs (inverted triangles), the production that occurs off that part of the shelf which is not upwind (south) of the bergs (triangles), and the shelf production that occurs upwind of the bergs (diamonds). On the bottom figure, the heavy lines show the cumulative production for 2000 and 2002.

Because K05's flux gate lies primarily over the continental shelf, we use only those measurements that lie between 100 and 600 km from the coast. This excludes the thin polynya ice adjacent to the coast and yields a mean thickness of 0.59 m with about a 50% standard deviation, where the standard deviation is much larger than K05′s estimate of a 3% error in the net outflow. To convert this saline ice thickness to a fresh water equivalent, we follow Haarpaintner et al. (2001), and assume that the young sea ice has a brine volume of 10 parts-per-thousand for a latent heat of freezing of about 300 kJ kg^{-1}, compared with the fresh water ice value of 334 kJ kg^{-1}. Multiplication of the thickness by the ratio of these two latent heats reduces the thickness to 0.53 m equivalent of fresh water ice, again with a 50% uncertainty.

Fig. 11 shows the yearly average winter ice production of the three polynyas, the total polynya yearly ice production, and the annual ice production inferred from K05. The figure also shows characteristic error bars both for our total ice production and for the K05 values. Examination of the lower part of the figure shows that the TNB and MAC ice production is approximately constant with time, while that of the RSP increases slowly through 1999, has a large increase in 2000, then decreases in 2001 and 2002. Its two smallest years are 1993 and 2002. A least squares fit to the data shows that the RSP ice production increases by 10 km^3 yr^{-1}. The mean winter total ice production of the western Ross polynyas is 500 ± 160 km^3, which includes the standard deviation associated with the heat flux uncertainty. For comparison, Jacobs et al. (2002), who apply mean winds and characteristic ice thicknesses to the width of the Ross Sea, estimate its annual ice export as 1000 ± 300 km^3, where the standard deviation is generated by the uncertainty in the ice thicknesses. With the uncertainties, the two estimates nearly overlap at 700 km^3.

The two solid curves in Fig. 11 compare the total production of the three polynyas with the production calculated from the K05 net outflow. The comparison shows that within the error bars, the two estimates are identical, and would remain so even if the SSM/I estimate is adjusted upward to account for the additional growth excluded by the 25-km pixel mask. Both estimates increase with time through 2001. Given the short decadal time period and the large variability in the annual ice production, this trend may not be significant, but it suggests that the observations of the HSSW salinity decline are associated not with a decrease in ice production, but rather in a salinity decrease in the properties of the seawater entering the Ross Sea from the east.

For comparison with the Ross Sea, in the Weddell Sea, there is a very different relation between the ice production and the ice export. Although the wind and ice circulation in the Weddell are similar to the Ross (Renfrew et al., 2002), the Weddell bottom topography is very different. Specifically, the shelf of the Weddell Sea is divided by the Berkner rise, which lies to the north of Berkner Island, has a minimum depth of 300–400 m, and extends to the continental shelf break. Because the rise is shallower than the characteristic ice shelf thickness of

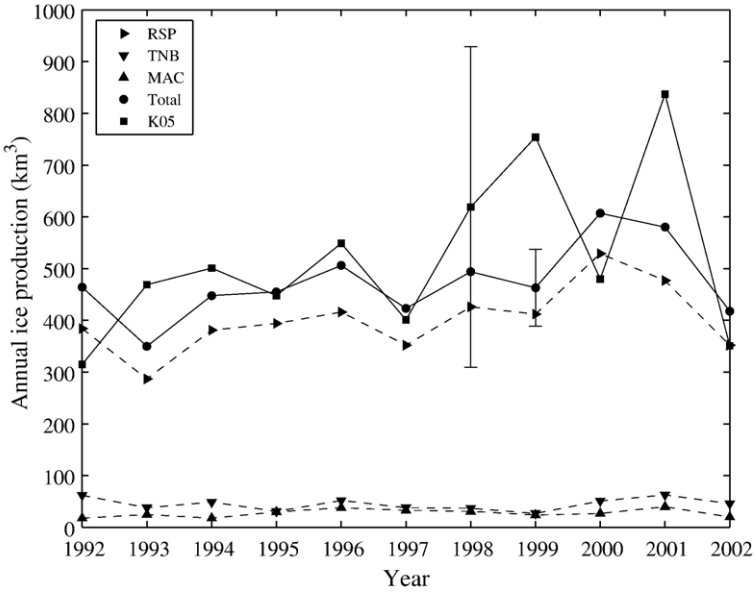

Fig. 11. The annual ice production for the RSP, TNB and MAC (dashed lines), the total annual ice production for these polynyas (solid line, black circles) and K05 ice production estimated from his areal export (solid line, black squares). The vertical lines show characteristic standard deviations for the Total and K05 cases. See inset box and text for further description.

400 m, icebergs tend to ground on it where they can remain for periods of order of a decade (Markus, 1996; Nøst and Østerhus, 1998; and contemporary satellite imagery at http://amrc.ssec.wisc.edu/iceberga.html). These grounded bergs block the east-to-west sea ice circulation that occurs in the Ross Sea and is associated with a large polynya productivity. Without taking these bergs into account, Arrigo and van Dijken (2003) show that the major polynya adjacent to the Ronne Ice Shelf has a mean winter area of about 5×10^3 km^2, compared with their 20×10^3 km^2 for the western Ross. Renfrew et al. (2002) show that the mean ice production of the Ronne polynya is about 100 km^3, compared with the Ross value of 500 km^3. More importantly, they show that the polynya ice production consists of only about 6% of the approximately 1800 km^3 of exported ice, whereas in the Ross, the ice export is in approximate balance with the polynya ice production. Because the above estimates for the Weddell do not account for the polynyas that form downwind of the grounded bergs, they may underestimate the ice production. Since both regions are important to the Antarctic bottom water production, these differences need further investigation.

6. Conclusions

For 1992–2002, we examined the ice production in the Ross Sea polynyas, using a passive microwave thin ice algorithm. To avoid sidelobe contamination, we masked both the ice shelf and in 2000–2002, the icebergs generated by the calving of B-15 and C-19. We then used the 10-cm isopleth from the thin ice algorithm to estimate the polynya areas, and combined with the meteorological data, the ice production. The areas and ice production of the polynyas are in approximate agreement with other investigators. Specifically, for ice production, our results are of the same order as the ice export estimate of Jacobs et al. (2002). Using an ice thickness derived from observation, our results agree with the K05 85-GHz net ice area export. We also show that in 2000 and 2002, the calving of large icebergs has a strong effect on the polynya ice production. Because the icebergs move with the currents and not the winds, first year ice builds up between the bergs and the ice shelf, and polynyas form downwind of the bergs. The ice trapped upwind of the bergs suppresses the ice production adjacent to the shelf, so that the center of the ice production and brine rejection can be moved from the shelf to the regions downwind of the bergs. Over our 11-year period, our ice production results show an increase in ice production with time. This suggests that the recent observations of the decline of the salinity of the HSSW is associated not with a decrease in ice production but rather with a salinity decrease in the properties of the water entering the Ross Sea from the east.

Acknowledgments

SM and RD gratefully acknowledge the support of NASA under contract number NNG04GM69G. The JPL effort was supported by NASA through a contract with the Jet Propulsion Laboratory, California Institute of Technology. The authors thank Miles Logsden and Leon Delwiche for their help in processing the MODIS data. We thank Doug MacAyeal for the 2001 and 2002 B-15A position data, and Stan Jacobs and Fred Davey for the bottom topography shown in Figs. 4 and 5. We also thank the National Snow and Ice Data Center in Boulder, CO for the daily averaged SSM/I data and the Alaska Satellite Facility for the SAR data.

References

Arrigo, K.R., van Dijken, G.L., 2003. Phytoplankton dynamics within 37 Antarctic coastal polynya systems. J. Geophys. Res. 108. doi:10.1029/2002JC001739.

Arrigo, K.R., van Dijken, G.L., Ainley, D.G., Fahnestock, M.A., Markus, T., 2002. Ecological impact of a large Antarctic iceberg. Geophys. Res. Lett. 29. doi:10.1029/2001GL014160.

Assmann, K.A., Timmermann, R., 2005. Variability of dense water formation in the Ross Sea. Ocean Dynamics 55, 68–87. doi:10.1007/s10236-004-0106-7.

Bromwich, D.H., Carrasco, J.F., Liu, Z., Tzeng, R.-Y., 1993. Hemispheric atmospheric variations and oceanographic impacts associated with katabatic surges across the Ross ice shelf, Antarctica. J. Geophys. Res. 98, 13,045–13,062.

Bromwich, D., Liu, Z., Rogers, A.N., Van Woert, M.L., 1998. Winter atmospheric forcing of the Ross Sea polynya. In: Jacobs, S., Weiss, R. (Eds.), Oceans, Ice, and Atmosphere: Interactions at the Antarctic Continental Margin, Antaract. Res. Ser., vol. 75. AGU, Washington, D.C., pp. 101–133.

Budillon, G., Pacciaroni, M., Cozzi, S., Rivaro, P., Catalano, G., Ianni, C., Cantoni, C., 2003. An optimum multiparameter mixing analysis of the shelf waters of the Ross Sea. Antarct. Sci. 15, 105–108.

Carmack, E.C., 1986. Circulation and mixing in ice covered waters. In: Untersteiner, N. (Ed.), The Geophysics of Sea Ice. Pergamon, Elmsford, NY, pp. 641–712.

Davey, F. J., 2004. Ross Sea Bathymetry, 1:2,000,000, version 1.0, Institute of Geological and Nuclear Sciences geophysical map 16, Institute of Geological and Nuclear Sciences Limited, Lower Hutt, New Zealand.

Doake, C.S.M., Corr, H.F.J., Rott, H., Skvarca, P., Young, N.W., 1998. Breakup and conditions for stability of the northern Larsen Ice Shelf, Antarctica. Nature 391, 778–780.

Drucker, R., Martin, S., Moritz, R., 2003. Observations of ice thickness and Frazil ice in the St. Lawrence Island Polynya from satellite imagery, upward looking sonar and salinity/temperature moorings. J. Geophys. Res. 108. doi:10.1029/2001JC001213.

Haarpaintner, J., Gascard, J.-C., Haugan, P.M., 2001. Ice production and brine formation in Storfjorden, Svalbard. J. Geophys. Res. 106, 14,001–14,014.

Hall, D.K., Key, J.R., Casey, K.A., Riggs, G.A., Cavalieri, D.J., 2004. Sea ice surface temperature product from MODIS. IEEE Trans. Geosci. Remote Sens. 42, 1076–1087.

Jacobs, S.S., Giulivi, C.F., 1998. Interannual ocean and sea ice variability in the Ross Sea. In: Jacobs, S., Weiss, R. (Eds.), Oceans, Ice, and Atmosphere: Interactions at the Antarctic Continental Margin, Antarct. Res. Ser., vol. 75. AGU, Washington, D.C., pp. 135–150.

Jacobs, S.S., Gordon, A.L., Ardai Jr., J.L., 1979. Circulation and melting beneath the Ross Ice Shelf. Science 203, 439–443.

Jacobs, S.S., Giulivi, C.F., Mele, P.A., 2002. Freshening of the Ross Sea during the late 20th century. Science 297, 386–389.

Jeffries, M.O., Adolphs, U., 1997. Early winter ice and snow thickness distribution, ice structure and development of the western Ross Sea pack ice between the ice edge and the Ross Ice Shelf. Antarct. Sci. 9, 188–200.

Keys, H.J.R., Jacobs, S.S., Barnett, D., 1990. The calving and drift of iceberg B-9 in the Ross Sea, Antarctica. Antarct. Sci. 2, 243–257.

Key, J.R., Collins, J., Fowler, C., Stone, R., 1997. High-latitude surface temperature estimates from thermal satellite data. Remote Sens. Environ. 61, 302–309.

Keys, H.J.R., Jacobs, S.S., Brigham, L.W., 1998. Continued northward expansion of the Ross Ice Shelf, Antarctica. Ann. Glaciol. 27, 93–98.

Kurtz, D.D., Bromwich, D.H., 1983. Satellite observed behavior of the Terra Nova Bay Polynya. J. Geophys. Res. 88, 9717–9722.

Kurtz, D.D., Bromwich, D.H., 1985. A recurring, atmospherically forced polynya in Terra Nova Bay. In: Jacobs, S.S. (Ed.), Oceanology of the Antarctic Continental Shelf, Antarct. Res. Ser., vol. 43. AGU, Washington, D.C., pp. 177–201.

Kwok, R., 2005. Ross Sea ice motion, area flux, and deformation. J. Clim. 18, 3759–3776.

Markus, T., 1996. The effect of the grounded tabular icebergs in front of the Berkner Island on the Weddell Sea ice drift as seen from satellite passive microwave sensors. IGARSS '96: Remote Sensing for a Sustainable Future, 1791–1793. IEEE Press, Piscataway, N.J., pp. 1791–1793.

Markus, T., Burns, B.A., 1995. A method to estimate subpixel-scale coastal polynyas with satellite passive microwave data. J. Geophys. Res. 100, 4473–4487.

Martin, S., Drucker, R., Kwok, R., Holt, B., 2004. Estimation of the thin ice thickness and heat flux for the Chukchi Sea Alaskan coast polynya from SSM/I data, 1990 – 2001. J. Geophys. Res. 108. doi:10.1029/2004JC002428.

Morales Maqueda, M.A., Willmott, A.J., Biggs, N.R.T., 2004. Polynya dynamics: a review of observations and modeling. Rev. Geophys. 42. doi:10.1029/2002RG000116.

Nøst, O.A., Østerhus, S., 1998. Impact of grounded icebergs on the hydrographic conditions near the Filchner Ice Shelf, Antarctica. In: Jacobs, S., Weiss, R. (Eds.), Ocean, Ice and Atmosphere: Interactions at the Antarctic Continental Margin, Antarct. Res. Ser., vol. 75. AGU, Washington, D.C., pp. 269–286.

Renfrew, I.A., King, J.C., Markus, T., 2002. Coastal polynyas in the southern Weddell Sea: variability of the surface energy budget. J. Geophys. Res. doi:10.1029/2000JC000720.

Van Woert, M.L., 1999. Wintertime dynamics of the Terra Nova Bay polynya. J. Geophys. Res. 104, 7753–7770.

Van Woert, M.L., Johnson, E.S., Langone, L., Worthen, D.L., Monaghan, A.J., Bromwich, D.H., Meloni, R., Dunbar, R.B., 2003. The Ross Sea circulation during the 1990s. In: Ditullio, G., Dunbar, R. (Eds.), Antarctic Research Series, Biogeochemical Cycles in the Ross Sea, Antarct. Res. Ser., vol. 78. AGU, Washington, D.C., pp. 5–34.

Zwally, H.J., Comiso, J.C., Gordon, A.L., 1985. Antarctic offshore leads and polynyas and oceanographic effects. In: Jacobs, S.S. (Ed.), Oceanology of the Antarctic Continental Shelf, Antarct. Res. Ser., vol. 43. AGU, Washington, D.C., pp. 203–226.